

PAPER • OPEN ACCESS

Conditions and benefits of X-point radiation for the island divertor

To cite this article: Y. Feng *et al* 2024 *Nucl. Fusion* **64** 086027

View the [article online](#) for updates and enhancements.

You may also like

- [Equilibrium effects on the structure of island divertor and its impact on the divertor heat flux distribution in Wendelstein 7-X](#)
S. Zhou, Y. Liang, A. Knieps et al.
- [Gas exhaust in the Wendelstein 7-X stellarator during the first divertor operation](#)
U. Wenzel, G. Schlisio, P. Drewelow et al.
- [Impact of nonlinear 3D equilibrium response on edge topology and divertor heat load in Wendelstein 7-X](#)
Y Suzuki and J Geiger

Conditions and benefits of X-point radiation for the island divertor

Y. Feng^{1,*} , V. Winters¹ , D. Zhang¹ , J. Geiger¹ , Y. Gao¹ , D. Reiter², P. Helander¹ , C.D. Beidler¹ , M. Endler¹ , D. Gradic¹, M. Jakubowski¹ , R. König¹, T. Kremeyer¹ , M. Krychowiak¹, D. Naujoks¹, M. Otte¹, V. Perseo¹ , F. Reimold¹, G. Schlisio¹  and the W7-X Team^{1,a}

¹ Max-Planck-Institut für Plasmaphysik, 17491 Greifswald, Germany

² Institute for Laser and Plasma Physics, Heinrich-Heine-University, D-40225 Duesseldorf, Germany

E-mail: feng@ipp.mpg.de

Received 15 March 2024, revised 23 May 2024

Accepted for publication 10 June 2024

Published 24 June 2024



Abstract

We present a method to geometrically quantify the three magnetic island chains with the poloidal mode numbers $m = 4, 5$, and 6 (referred to in this paper as high-iota, standard, and low-iota islands, respectively), on which the W7-X divertor relies. The focus is on a comparative study of their detachment performance using a series of models of different physical and geometrical complexity, ranging from one- to three-dimensional (1D to 3D). In particular, it aims to identify the key physical elements behind the correlation between impurity radiation and island geometry and the associated detachment stability. Assuming intrinsic carbon as a radiator, we scan the three island chains with the EMC3-Eirene code based on otherwise identical code inputs. We find that the three islands behave differently in the radiation distribution, in the development of the radiation zones during detachment, and in the ‘radiation costs’, defined as the product of impurity and electron density near the last closed flux surface. While the radiation costs for the $iota = 5/4$ and $5/5$ island chains linearly increase with the total radiation, the low-iota island with $iota = 5/6$ shows a bifurcation behavior in the sense that the radiation costs initially increase and then decrease when the total radiation exceeds a critical level. Consistent with the numerical trends, stable detachment, which is experimentally easy and robust to achieve with the standard $iota = 5/5$ island chain, remains an experimental challenge with the low-iota configuration. Dedicated numerical experiments show that the recycling neutrals and the ratio of parallel to perpendicular heat transport, which depends closely on the field line pitch, play a significant role in the formation and evolution of the radiation layer. A deeper understanding of the underlying physics relies on simpler models that explain why and how flux expansion can reduce the radiation costs. From these insights, we derive the conditions in which detached plasmas can benefit from the expansion of flux surfaces around the X-point. We show and explain why the current divertor design limits the actual capability of the high-iota configuration and propose solutions. The work is presented within a theoretical/numerical framework but cites relevant experimental evidence to emphasize its practical significance.

^a See Grulke *et al* 2024 (<https://doi.org/10.1088/1741-4326/ad2f4d>) for the W7-X Team.

* Author to whom any correspondence should be addressed.



Original Content from this work may be used under the terms of the [Creative Commons Attribution 4.0 licence](https://creativecommons.org/licenses/by/4.0/). Any further distribution of this work must maintain attribution to the author(s) and the title of the work, journal citation and DOI.

Keywords: W7-X, island divertor, EMC3-Eirene, detachment stability, X-point radiation

(Some figures may appear in colour only in the online journal)

1. Introduction

The success in the construction and operation of W7-X [1] and the first experimental results [2–5] have renewed interest in stellarators and triggered great efforts to optimize the stellarator concept [6]. W7-X is highly optimized concerning neo-classical transport [7, 8]. The divertor was not an optimization target but was later developed based on the natural edge magnetic islands [9]—the so-called island divertor, after a successful pre-test on its predecessor W7-AS [10–13]. Given that plasma exhaust concepts in stellarators heavily rely on the intrinsic magnetic field structure at the edge of each configuration [14], further stellarator concepts must incorporate a viable solution for plasma exhaust in the optimization process.

The island divertor may be viewed as a customized plasma exhaust concept for the low-shear and current-less W7-stellarators. However, magnetic islands are inherently present at the edge of all non-axisymmetric (helical) devices unless the plasma is limited by a wall component. Regarding the magnetic field topology at the edge, helical devices differ in which and how many island chains form a scrape-off layer (SOL), depending on the iota profile and the field spectrum of the 3D coils in each device. The large helical device LHD [15] has a high magnetic shear, and the SOL is composed of a number of island chains that overlap and form a ‘stochastic’ layer at the edge. From the viewpoint of iota-profile and magnetic shear, the low-shear stellarator W7-X and the high-shear helical device LHD should be the two extremes, and other types of helical devices should fall somewhere in between. LHD is exploring a so-called helical divertor [16], in which low-order magnetic islands play an important role in the SOL transport [17, 18]. Although the two divertors differ significantly in the divertor geometry, they share many similarities in the divertor transport [19–22]. Therefore, the knowledge gained from the island and helical divertors should be valuable for any 3D divertor concept under consideration, including the recently proposed ‘non-resonant’ divertor [23, 24]. The term ‘non-resonant’ is still controversial since the SOL plasma transport actually depends heavily on low-order resonances.

One of the design metrics for a divertor is the capability of stable operation of a highly dissipative plasma, known as ‘detachment’ [25–28]. Divertor experiments from W7-AS, W7-X, and LHD consistently showed that stable detachment requires large magnetic islands with strong perturbation fields [29–33]. This cross-machine result demonstrates the importance of magnetic islands for the performance of 3D divertors. Although the underlying physics is not fully clear, EMC3-Eirene modeling for all three devices has shown that the distribution of impurity radiation closely correlates with the island geometry, which is in line with experimental observations. In particular, experiments and modeling have shown

that stable detachment conditions achieved at LHD and W7-X are associated with significant X-point radiation (XPR) [31, 32, 34–38]. XPR is also a topic of renewed intense interest to the tokamak community as a potential power dissipation regime for future tokamaks [39–41].

Thanks to the high flexibility of the magnetic field configuration [42], W7-X offers an ideal test bed for investigating geometric effects of the edge magnetic islands on the impurity radiation distribution and the associated detachment stability. Divertor experiments have shown that stable detachment, which is easy and robust to access for the standard island chain [35, 43–45], is difficult to achieve with the low-iota island [33]. This experimental finding immediately drew great attention to the low-iota island in order to understand why and how the island geometry can affect the stability of detached plasmas in W7-X. EMC3-Eirene simulations covering a range of plasma parameters and cross-field transport coefficients showed the presence of intense radiation inside the low-iota island near the O-point [33], which is fundamentally different from the XPR feature realized for the standard island chain so far [34–36]. The work in this paper is a continuation of earlier studies towards a deeper and more comprehensive understanding of the fundamental physics behind the geometric effects on the island divertor performance.

In the next section, we introduce and determine the crucial geometric parameters of the three different chains of magnetic islands. 3D simulations are presented and discussed in section 3. Section 4 introduces simpler models to describe flux expansion effects. Section 5 derives the conditions required for XPR and explains why larger islands are beneficial. In section 6, we summarize the main results.

2. Quantification of magnetic islands

Magnetic islands can be described analytically when assuming a constant magnetic shear $\iota' = d\iota/dr$ around a rational magnetic surface [46, 47], where r is the so-called effective radius of a closed flux surface and $\iota = d\theta/d\phi$ is the rotational transform and describes how fast a field line changes its poloidal angle θ relative to the toroidal angle ϕ in Boozer coordinates. Obviously, evaluating the geometrical parameters in a realistic magnetic configuration requires the use of magnetic coordinates that describe nested magnetic flux surfaces without the island-generating resonant field component. In this section, we derive and determine the geometric parameters relevant to this work.

First, we extend the description of the island surfaces in [47] to the disturbed magnetic surfaces outside the magnetic island, which are relevant to the topic of impurity radiation addressed in this work. Denoting magnetic surfaces outside the island by

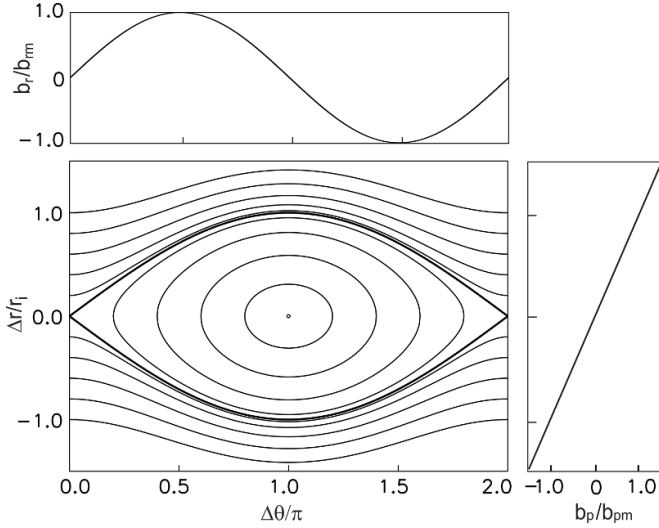


Figure 1. Perturbed magnetic surfaces (left bottom) by a resonant radial field component (top) in combination with a finite magnetic shear (right bottom), as described by equation (1). The magnetic surfaces outside the island are created by changing $\Delta r_0/r_i$ from ± 0.2 to ± 1 with the step of ± 0.2 , while setting $\Delta\theta_0$ to be zero. The surfaces inside the island are obtained by varying $\Delta\theta_0$ from 0.2π to π with the step of 0.2π at $\Delta r_0 = 0$. The separatrix (thicker line) corresponds to $\Delta r_0 = \Delta\theta_0 = 0$.

$\Delta r_0 = r_0 - r_a$, where r_a labels the undisturbed rational surface, equation (6) in [47] becomes

$$\Delta r = \pm \sqrt{(\Delta r_0)^2 + r_i^2 \cdot \frac{\cos(\Delta\theta_0) - \cos(\Delta\theta)}{2}} \quad (1)$$

where $\Delta\theta = m\theta - n\phi$, $\Delta\theta_0$ ranges from 0 to π and labels the island surfaces, and

$$r_i = 2\sqrt{\frac{R \cdot b_{rm}}{\epsilon' \cdot m}} \quad (2)$$

is known as the half-width of the island. In equation (2), R is the major radius, b_{rm} is the magnitude of the resonant radial field component that creates the magnetic island, ϵ' is the magnetic shear, and m is the poloidal mode number. The magnetic flux surfaces described by equation (1) are illustrated in figure 1, including the perturbation field $b_r = b_{rm}\sin(\Delta\theta)$ and the divertor-relevant poloidal field component $b_p = (r_a/R) \cdot \epsilon' \cdot \Delta r$ normalized to $b_{pm} = 4r_a \cdot b_{rm}/(m \cdot r_i)$ (see detailed explanations in [47]) under the assumption of constant magnetic shear and b_{rm} . Both b_r and b_p are normalized to the toroidal field. The separatrix of the magnetic island is defined by $\Delta r_0 = 0$ and $\Delta\theta_0 = 0$. The magnetic surfaces outside the island are described by setting $\Delta\theta_0 = 0$. Setting $\Delta r_0 = 0$ instead, equation (1) reduces to equation (6) in [47] for the island surfaces.

The magnetic surfaces around the X-point are farther apart than those away from the X-point, figure 1. For example, the radial distance of a perturbed magnetic surface with a finite value of Δr_0 to the separatrix, s , varies with $\Delta\theta$ as

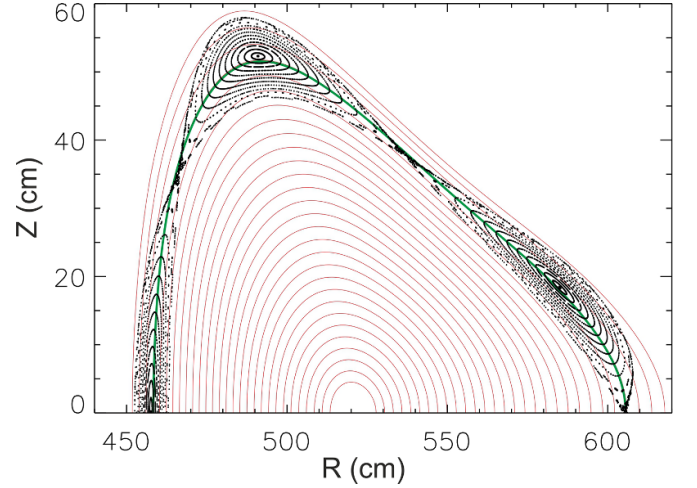


Figure 2. The standard $\iota = 5/5$ (vacuum) magnetic configuration of W7-X in an up/down symmetric triangular plane. Red: magnetic flux surfaces from VMEC; green: the $\iota = 5/5$ resonance; black: Poincare plot of the island chain calculated from the coils.

$$s(\Delta\theta) = \sqrt{(\Delta r_0)^2 + r_i^2 \cdot \frac{1 - \cos(\Delta\theta)}{2}} - \sqrt{r_i^2 \cdot \frac{1 - \cos(\Delta\theta)}{2}} \quad (3)$$

and has a maximum at $\Delta\theta = 0$ (flux expansion) and a minimum at $\Delta\theta = \pi$ (flux compression). Effects of magnetic flux expansion on impurity radiation are studied in section 4.

One of the most important geometric parameters is the internal field line pitch $\Theta \approx \sqrt{b_r^2 + b_p^2}$ under the approximation of $B \approx B_r$, which determines the projection of parallel heat and particle fluxes on a ϕ -plane and thus controls their relative weight to perpendicular transport. This field line pitch is one of the key factors that makes the detachment performance of the three island chains so different.

In order to determine the geometric parameters described above, we need the r -coordinates, which describe the undisturbed magnetic flux surfaces. The equilibrium code VMEC [48] assumes nested magnetic flux surfaces, and excludes the existence of magnetic islands, providing a good approximation. Using the standard island chain (vacuum field) as an example, figure 2 shows the magnetic flux surfaces (marked in red) calculated by VMEC practically with no plasma pressure. The green surface is the $\iota = 5/5$ resonance. The superimposed Poincare plots are provided independently by EMC3-Lite [47] through Biot-Savart calculation of the magnetic fields directly from the coil currents. The good quality of the VMEC surfaces for assessing the island geometry is reflected by the small deviations of the O-points and X-points from the green rational surface. The deviations are much smaller than the island size. The radial island width W_r is determined by finding the maximum and minimum values of the radial coordinates of the island separatrix. The radial coordinates are obtained through cylindrical approximation of the volume enclosed by the VMEC surfaces. VMEC also provides the iota profile. The results for the three vacuum island chains

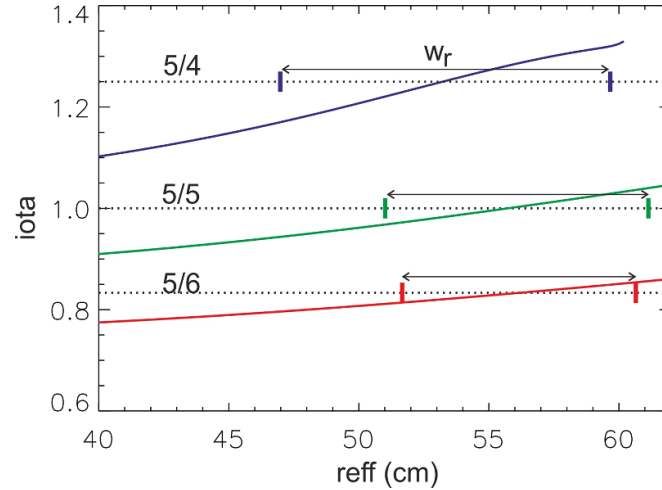


Figure 3. Iota profiles and the island widths of the three island chains.

Table 1. Island geometric parameters in vacuum fields.

Conf.	m	r_a (cm)	shear (cm^{-1})	W_r (cm)	W_p (cm)	L_{co} (m)	b_{rm}	b_{pm}
Low iota	6	56	4.4×10^{-3}	9.0	59	590	2.4×10^{-4}	2.0×10^{-3}
Standard	5	56	7.1×10^{-3}	10.6	70	370	4.5×10^{-4}	3.8×10^{-3}
High iota	4	53	1.2×10^{-2}	13	83	230	8.8×10^{-4}	7.4×10^{-3}

are displayed in figure 3, where the iota profiles are shown only for the edge region of interest. The magnetic shear for each configuration is determined by differentiating the iota values at the outermost and innermost radial positions of the island.

Once the magnetic shear and the radial island size are known, all other geometric parameters can be derived and are listed in table 1. For completeness, the location of the rational surface— r_a , the poloidal island width W_p , and the connection length $L_{co} = (\pi/2)W_r/b_{rm}$ (the field line length to complete an internal poloidal turn at the O-point) are also given.

In general, the perturbation field b_{rm} increases with iota. The increase in $b_{pm} = (r_a/R) \cdot \epsilon' \cdot r_i$ with iota is mainly due to the increased magnetic shear. These two parameters determine Θ . Note that the ratio of parallel to perpendicular conductive heat flux is proportional to Θ squared [22, 49].

3. EMC3-Eirene modeling

The EMC3-Eirene code consists of a reduced set of time-independent fluid equations for electrons, ions, and impurities, and a kinetic model for neutral gas [50, 51]. The current code version is not capable of a self-consistent treatment of cross-field drifts. Nevertheless, the code was able to reproduce many general aspects of the experimentally observed detachment [35, 36, 44], which encourages us to look for further physical effects to which the current code version is applicable.

3.1. Simulation results with impurity transport

The EMC3-Eirene code includes a reduced fluid model for impurity transport, consisting of continuity and a simplified momentum balance, taking only into account the parallel classical forces [52]. The cross-field transport is purely diffusive, and the diffusivity is a free input parameter, which usually takes the same value as that for the background ions since it is difficult to determine experimentally. Impurities affect the background plasma only through energy losses in the excitation and ionization processes. Herein, they are collectively referred to as P_{rad} . Regarding detachment, the standard island chain is the most studied configuration, both theoretically and experimentally. Although many aspects of the W7-X detachment have been studied using the EMC3-Eirene code, the stability of a detached plasma was not explored until it was recently found that stable detachment—a robust, routinely operated regime for the standard island—proved hard to achieve with the low-iota island chain [33]. After the detachment transition, the plasma in this magnetic configuration usually evolved into an oscillating state. EMC3-Eirene simulations under different assumptions for cross-field transport showed qualitatively a nearly invariant radiation distribution with strong radiation peaks occurring somewhere in the island region between the neighboring X-points [33], which is not the case for the standard island. As a typical example for the standard island, figure 4 shows the distribution and development of carbon radiation with rising the radiation fraction $f_{rad} = P_{rad}/P_{SOL}$ (P_{SOL} = the total power entering the simulation domain), reproduced from [36]. Shown are three carbon

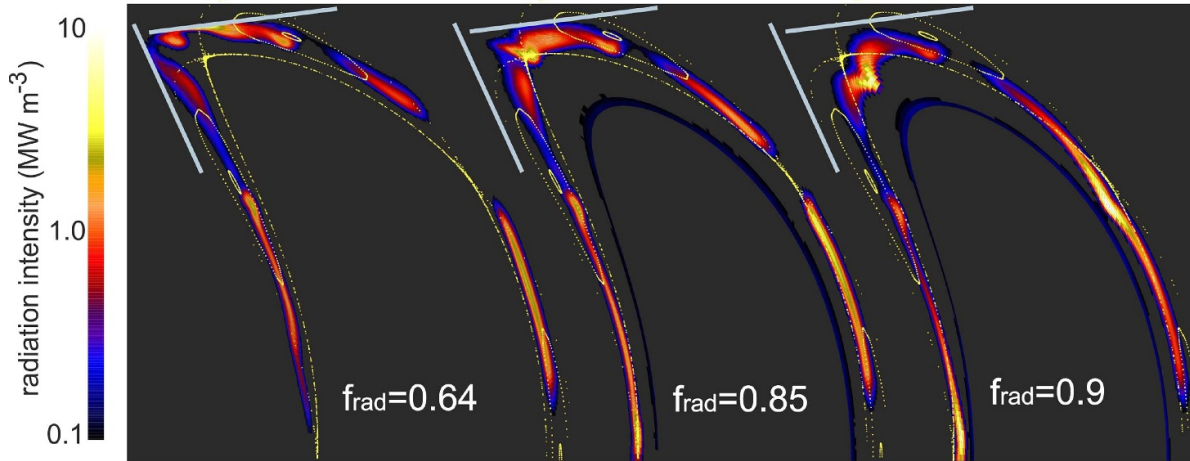


Figure 4. Carbon radiation distributions in a bean-shaped plane for the standard island at $f_{\text{rad}} = 0.64, 0.85,$ and 0.9 with the corresponding densities of $n_{\text{IBS}} = 5.0, 5.4,$ and $5.5 \times 10^{19} \text{ m}^{-3}$. Other input parameters are $P_{\text{SOL}} = 5 \text{ MW}$, $D = 0.5 \text{ m}^2 \text{ s}^{-1}$, and $\chi_e = \chi_i = 0.75 \text{ m}^2 \text{ s}^{-1}$. Reproduced from [36]. © EURATOM 2021 CC BY 3.0.

radiation distributions at $f_{\text{rad}} = 0.64, 0.85,$ and 0.9 , respectively, with the corresponding plasma densities at the innermost boundary surface of the EMC3 domain (0.84 of the minor radius), $n_{\text{IBS}} = 5.0, 5.4,$ and $5.5 \times 10^{19} \text{ m}^{-3}$. Due to the lack of quantitative knowledge of carbon release processes in W7-X, it is assumed that the carbon yield is proportional to the flux of the background ions on the graphite target to account for chemical sputtering processes relevant to the detached plasmas studied in this work. Carbon atoms are started from the graphite target with an initial energy of 0.1 eV . Other input parameters are $P_{\text{SOL}} = 5 \text{ MW}$, which is divided equally between the electrons and ions, $D = 0.5 \text{ m}^2 \text{ s}^{-1}$ (cross-field particle diffusivity for both carbon and hydrogen), $\chi_e = \chi_i = 0.75 \text{ m}^2 \text{ s}^{-1}$ (cross-field heat conductivity of electrons and ions). At $f_{\text{rad}} = 0.64$, intense radiation first appears near the strike-line. As the impurity radiation increases, the radiation then moves along the outer separatrix (divertor leg) toward the X-point, eventually entering the confinement region through the X-point, hence the name ‘XPR’. Two secondary radiation peaks occur around the centers of the top and inboard islands, but do not contribute significantly to the total radiation due to their limited size and lower intensity. Note the logarithmic scale in figure 4. The two peaks are located poloidally at the stagnation of the background plasma flow and are thus related to the impurity transport, which we will come back to later.

In order to illustrate the essential difference in the radiation distribution between the standard and the low-iota island, we show here a simulation example for the low-iota island. Further examples can be found in [33]. To allow a direct comparison of the two island chains, the same f_{rad} scan performed for the standard island depicted in figure 4 is repeated for the low-iota island. The results are illustrated in figure 5, which shows the carbon radiation distributions in the low-iota island with (a) $f_{\text{rad}} = 0.7$ and $n_{\text{IBS}} = 5.1 \times 10^{19} \text{ m}^{-3}$, and (b) $f_{\text{rad}} = 0.85$ and $n_{\text{IBS}} = 5.4 \times 10^{19} \text{ m}^{-3}$ respectively. In contrast to the XPR pattern in figure 4 for the standard island, figure 5 for the low-iota island shows two main radiation peaks in the

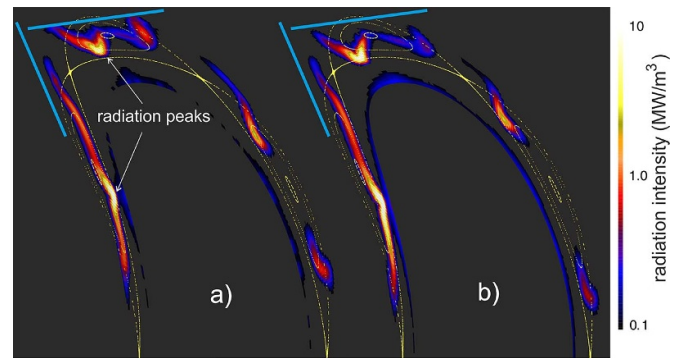


Figure 5. Carbon radiation distributions for the low-iota island with (a) $f_{\text{rad}} = 0.7$, $n_{\text{IBS}} = 5.1 \times 10^{19} \text{ m}^{-3}$, and (b) $f_{\text{rad}} = 0.85$, $n_{\text{IBS}} = 5.4 \times 10^{19} \text{ m}^{-3}$. The other input parameters are the same as those in figure 4.

top and inboard islands, respectively, between neighboring X-points. To distinguish this radiation pattern from the XPR pattern of the standard island, we will refer to it as ‘O-point radiation’ in this paper, although it is not really localized at the O-point. As f_{rad} increases, the radiation layer moves inward toward the last closed flux surface (LCFS), and the radiation front eventually reaches the LCFS at $f_{\text{rad}} = 0.85$, figure 5(b). Above this radiation level, the EMC3-Eirene code, which is based on fixed-point iteration, cannot find a solution. During iteration, the total radiation does not converge to a fixed point, but oscillates around a radiation level clearly above it.

In summary, detachment simulations for the low-iota island covering a range of input parameters generally show radiation peaks inside the low-iota islands in front of the targets. So far, no solution could be found when the radiation front enters the confinement region.

We cannot rule out possible numerical issues. However, there are good reasons and evidence pointing to physical effects. First, for the standard island with otherwise identical settings, converged solutions exist up to f_{rad} levels where the

radiation is mainly inside the LCFS. Second, physical solutions to the strongly nonlinear system addressed by EMC3-Eirene are not guaranteed to exist everywhere in the spaces of plasma parameters and divertor configurations, especially given the high T_e -sensitivity of atomic reaction rates under detached, low- T_e conditions. For the standard island, as f_{rad} increases, the EMC3-Eirene code shows a smooth transition of the radiation layer across the X-point into the confinement region—figure 4. It would be very interesting to see how the radiation pattern in figure 5(b) further develops at a higher f_{rad} , but this is unfortunately inaccessible for the current models used. Even if we were convinced that there is a close connection between the numerical event and the experimental unstable detachment for the low-iota island, we cannot understand the underlying physics without finding a numerical solution. An alternative is therefore needed.

3.2. Exploration of a suitable impurity radiation model

The EMC3-Eirene modeling performed in [33] has shown that the ‘O-point’ radiation pattern in the low-iota chain is robust to transport and species of impurities. This numerical finding motivates us to consider a simpler model for impurity radiation. In fact, impurity radiation is most sensitive to the electron temperature, and such radiation properties can be described by cooling rate functions. With these considerations in mind, we explore an impurity concentration model to replace the more complicated impurity transport model of EMC3. Here, the only constraint is that the model must be able to reproduce the main features of the radiation distribution predicted by the impurity transport model and at the same time provide solutions for all three islands over the entire parameter range of interest, so that we can study the different islands with a unified physical model.

We assume that the impurity density is everywhere proportional to the background plasma density as $n_I = c \cdot n$ where c is the impurity concentration and $n \equiv n_e = n_i$. Although impurity transport is not explicitly included, the associated effects on radiation are implicitly taken into account to some extent by assuming non-coronal equilibrium radiation functions. The impurity radiation intensity R_z reads

$$R_z(n, T_e) = c \cdot n^2 \cdot L_z(T_e) \quad (4)$$

and is only a function of c , n and T_e . There, L_z is the so-called cooling rate and depends only on T_e . Figure 6 shows three cooling rates as a function of the electron temperature, marked as Cr^a , Cr^b , and Cr^c , respectively. The rate Cr^c is calculated for carbon at coronal equilibrium based on ADAS database, serving only as a reference here. The cooling rate Cr^a is obtained for carbon from some detachment simulations of W7-X in such a way that the resulting temperature spectrum of the radiation is averaged in logarithmic space over the radiation intensity with a $\log_{10} T_e$ resolution of 0.1 and then fitted with a cubic spline. There, the shift of the peak radiation to a higher T_e point and the broader radiation profile compared to Cr^c are due to transport effects. The cooling rate Cr^b is

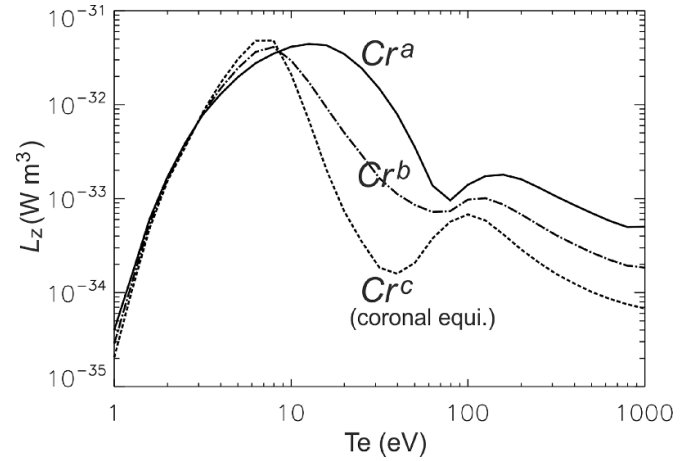


Figure 6. Two different cooling rate functions marked by Cr^a (solid) and Cr^b (dot-dashed) used in simulation. The dashed curve Cr^c is the coronal equilibrium, shown only for reference.

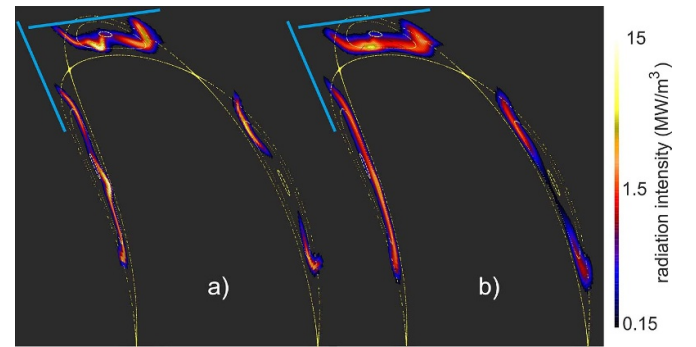


Figure 7. Radiation distributions calculated for the low-iota island based on the radiation rate Cr^b (left) and Cr^a (right), respectively. Other input parameters are identical to those for figure 5(a).

the (geometric) average of Cr^a and Cr^c in logarithmic space, i.e. $\log Cr^b = (\log Cr^a + \log Cr^c)/2$. The choice of these cooling rates is not further justified other than by the criteria mentioned at the beginning of this section. In other words, this choice can be regarded as an attempt, and the applicability of the cooling rate functions will then be evaluated based on their performance in generating the radiation distributions. First, we apply the concentration model to the standard and low-iota island chains since they are the most studied divertor configurations regarding detachment. The other input parameters are identical to those taken to produce figure 5(a). Figures 7(a) and (b) display the results for the low-iota island using the Cr^b and Cr^a cooling rates, respectively. Compared to the radiation distribution depicted in figure 5(a), figure 7(a) exhibits more similar features than figure 7(b). The two separate radiation zones in the top and inner islands in figure 7(a) merge into a single one in figure 7(b). In the latter case, most of the fine structures disappear. Up to the accuracy level of the effects discussed in this paper, all three radiation patterns are equivalent, since they all possess the basic properties of the so-called ‘O-point radiation’ described above.

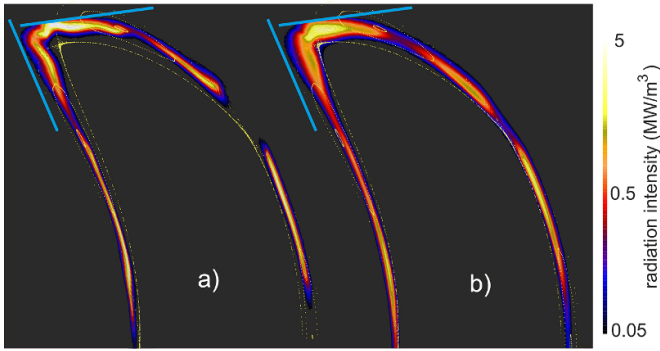


Figure 8. Same as figure 7, but for the standard island chain.

The radiation pattern changes qualitatively after switching from the low-iota island to the standard divertor configuration, as can be clearly seen in figure 8. Note that the magnetic configuration is the only parameter that was changed in the modeling when comparing figures 7 and 8 pairwise. Radiation now occurs mainly on the island periphery or even in the private flux region, which qualitatively agrees well with the ‘XPR’ map realized for the standard island so far. The two secondary radiation peaks seen in figure 4 now disappear from figure 8 after replacing the impurity transport model with the concentration model.

The better match between figures 5(a) and 7(a) indicates that the radiation model Cr^b provides a better approximation to the impurity transport model than Cr^a . On the other hand, and probably for this very reason, this radiation model has difficulty in finding a converged solution in the high radiation range, similar to the case of the impurity transport model. By contrast, as will be discussed in detail in the next section, stable solutions can be found with the Cr^a cooling rate throughout the entire detachment phase of interest. For this reason, in the following all EMC3-Eirene simulations will be carried out using the Cr^a cooling rate function.

3.3. Main 3D simulation results

Based on the concentration model—equation (4)—with the cooling rate Cr^a , we perform a series of radiation scan for the three island chains and use the quantity of $c \cdot n_{\text{IBS}}^2$ to evaluate the ‘radiation costs’. The innermost boundary surface (IBS) is located about eight centimeters inside the LCFS to allow full development of the radiation distribution within the LCFS at deep detachment, so uncertainties in boundary conditions do not enter our discussions. Although the simulations in this work do not target any specific discharges, for continuity purposes, the computational setup is largely based on what was taken in our previous work on the standard island chain [36] and justified in [53]. We assume hydrogen plasmas with a spatially constant $D = 0.5 \text{ m}^2 \text{ s}^{-1}$. P_{SOL} is set to be 5 MW unless explicitly stated in certain cases. The anomalous heat conductivities of electrons and ions are co-varied as $\chi_e = \chi_i$ in the range from 0.5 to $1.5 \text{ m}^2 \text{ s}^{-1}$, either to check sensitivity or physical effects. The radiation fraction f_{rad} is used as a control parameter so that the impurity concentration c is a code

output. The plasma density at the IBS, n_{IBS} , is co-varied with f_{rad} in the range of $5\text{--}5.5 \times 10^{19} \text{ m}^{-3}$. This n_{IBS} fine-tuning may not be necessary but should better reflect reality.

The simulation results for the three island chains with $\chi = 0.75 \text{ m}^2 \text{ s}^{-1}$ are summarized in figure 9, where f_{rad} is plotted against $c \cdot n_{\text{IBS}}^2$ on the left side. For the standard and high-iota islands, f_{rad} increases almost linearly with $c \cdot n_{\text{IBS}}^2$. In contrast, a non-linear behavior occurs for the low-iota island at $f_{\text{rad}} > 0.8$, where f_{rad} changes its slope from positive to negative, indicating a bifurcation tendency. In figure 9(a), each f_{rad} -curve starts at the same $f_{\text{rad}} = 0.64$ point but ends at a different f_{rad} -value. This is because in each case the f_{rad} scan is stopped when the radiation on the closed field lines starts to dominate—figure 9(b). Independently of the divertor configuration, increasing f_{rad} in the detachment phase always causes a radial movement of the radiation layer toward the confinement region. The location of the radiation layer with respect to the LCFS can be characterized by determining the proportion of radiation within the LCFS R_{core} relative to the total radiation R_{total} , denoted by f_{core} . The corresponding f_{core} values during the scans are plotted against f_{rad} in figure 9(b). Not surprisingly, f_{core} behaves differently for the different island chains. However, the markedly different behavior of f_{core} of the high-iota island from the other two islands is not understandable at first glance. About 30% of the radiation originates inside the LCFS already at $f_{\text{rad}} = 0.64$ —a radiation level at which the radiation layer usually starts to detach from the targets. Faced with this puzzle, we carefully reviewed the current W7-X divertor design and noted that it is unsuitable for exploring the actual potential of the high-iota island in terms of its detachment performance. The reason for this will be given in the next section. Below in this section, the high-iota island drops out of our island scan study.

The change of the f_{rad} -slope in the low-iota island chain occurs during the transition of the radiation layer from the SOL into the confinement characterized by a ‘jump’ of f_{core} from 0.1 to 0.6, as f_{rad} increases from 0.85 to 0.9. This jump in f_{core} results from a significant redistribution of the impurity radiation, as illustrated in figure 10, which compares the radiation distributions at $f_{\text{rad}} = 0.85$ and 0.9, respectively. For a more complete look at the evolution of the radiation distribution, we include figure 7(b) in our discussion, which is taken at $f_{\text{rad}} = 0.7$ from the same f_{rad} -scan. Increasing f_{rad} from 0.7 in figure 7(b) to 0.85 in figure 10(a) does not lead to significant changes in the radiation pattern, but mainly to an inward shift of the radiation location, which is still outside but already very close to the LCFS—figure 10(a). However, a further but much smaller increase in f_{rad} from 0.85 to 0.9 causes a drastic change in the radiation pattern—figure 10. Now the radiation is more concentrated near the X-points and forms peaks in front of them inside the LCFS—a radiation pattern similar to what is known as the ‘XPR’. The poloidal redistribution of the radiation is associated with the radial inward movement of the radiation layer. As the radiation layer moves inward into the confinement area, the b_p field in the radiation flux tube increases (figure 1) so that a sufficient amount of power can be transferred to the radiation zone in front of the X-point. More details on this are discussed in section 5. The evacuation of

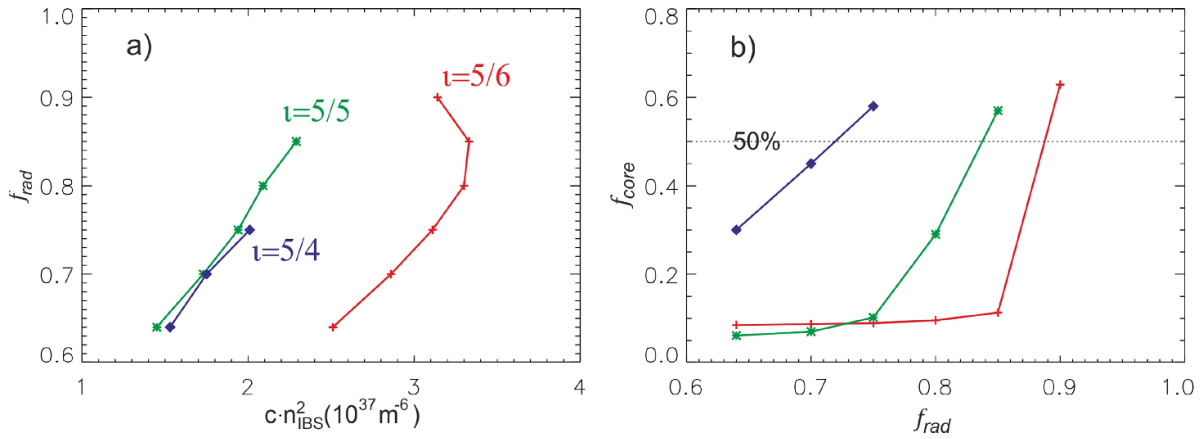


Figure 9. (a) Correlations between carbon radiation and the radiation costs with $\chi = 0.75 \text{ m}^2 \text{ s}^{-1}$ for the standard (green), low-iota (red), and high-iota (blue) islands. (b) The corresponding radiation fractions within the LCFS as a function of f_{rad} .

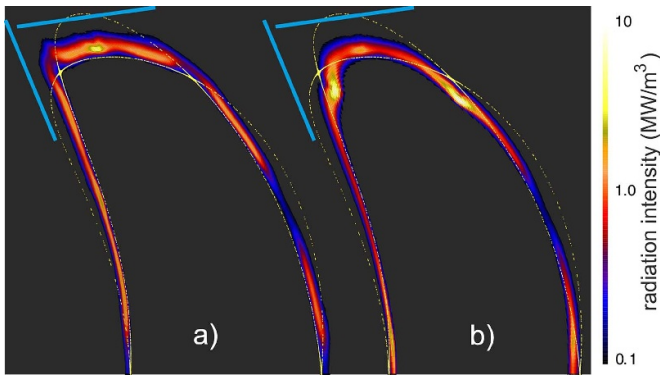


Figure 10. Radiation distributions for the low-iota island at (a) $f_{\text{rad}} = 0.85$, $n_{\text{IBS}} = 5.4 \times 10^{19} \text{ m}^{-3}$, and (b) $f_{\text{rad}} = 0.9$, $n_{\text{IBS}} = 5.5 \times 10^{19} \text{ m}^{-3}$.

radiation from the island region leads to the negative f_{rad} -slope shown in figure 9(a), which means that the plasma density or the impurity concentration or both need to be reduced in the confinement region when f_{rad} increases from 0.85 to 0.9.

For comparison, figure 11 illustrates how the radiation distribution in the standard island evolves as the radiation layer enters the confinement region. Similar to the discussions for the low-iota island, we include figure 8(b) to our discussion for the standard island. Figure 8(b) together with figures 11(a) and (b) show a clearly different map of movement for the radiation layer. It enters the confinement region through the X-points and this does not lead to any change in the f_{rad} -slope—figure 9(a).

The simulations discussed above are repeated by doubling χ to $1.5 \text{ m}^2 \text{ s}^{-1}$ and the results are depicted in figure 12. Comparing with figure 9, there are no notable qualitative differences, but there are quantitative differences in many aspects. First, the detachment operation windows of $c \cdot n_{\text{IBS}}^2$ for both island chains become narrower. Second, the radiation layer enters the confinement domain at lower f_{rad} values. Third, bifurcation occurs in the low-iota island at a lower f_{rad} point, and f_{rad} becomes more sensitive to $c \cdot n_{\text{IBS}}^2$ in the entire analysed phase.

In the high f_{rad} range from 0.85 to 0.9, the $f_{\text{rad}} - c \cdot n_{\text{IBS}}^2$ curve of the low-iota island changes its slope once again, now from negative to positive, figure 12(a). At $f_{\text{rad}} = 0.9$, f_{core} reaches about 0.75 (figure 12(b)), and the radiation front penetrates deep into the confinement area. Flattening effects of f_{rad} in relation to $c \cdot n_{\text{IBS}}^2$ in the high f_{rad} range, where f_{core} is significantly above 0.5, are also seen for the standard island chain with either $\chi = 0.75$ or $1.5 \text{ m}^2 \text{ s}^{-1}$. Independent of the island configuration, EMC3-Eirene simulations generally show a positive correlation between f_{rad} and $c \cdot n_{\text{IBS}}^2$ when the radial layer is located predominantly within the LCFS. It is not clear to what extent the SOL plasma transport code, EMC3-Eirene, is applicable to these situations. However, this numerical trend is consistent with the flux expansion effect described later in this paper.

To further investigate the causes for the bifurcation, we add two more scans with a lower $\chi = 0.5 \text{ m}^2 \text{ s}^{-1}$ and a lower $P_{\text{SOL}} = 3 \text{ MW}$, respectively. To facilitate an overview, all scans resulting from the low-iota island are summarized in figure 13. In figure 13(a), $c \cdot n_{\text{IBS}}^2$ is normalized to its value at $f_{\text{rad}} = 0.75$, which is given in the figure legend, in order to emphasize its relative change, i.e. sensitivity. These results show a general tendency that, as the ratio of parallel to perpendicular transport increases, the bifurcation shrinks in the $c \cdot n_{\text{IBS}}^2$ range and shifts to higher f_{rad} -values, but does not disappear. In the next section, we proceed to discuss the recycling neutrals—another important factor that affects the radiation distribution.

3.4. The role of recycling neutrals in plasma condensation

Recycling neutrals provide particle sources and energy sinks to the background plasma due to ionization, excitation and dissociation processes, and thus can induce plasma condensation in the presence of impurity radiation [39]. Volume recombination processes are not taken into account in this work. The contribution of electron-ion recombination turned out to be not really relevant for W7-X under the conditions achieved so far [36]. Given the relatively low plasma and molecular density in the island divertor (see justification in [36]), it is expected that

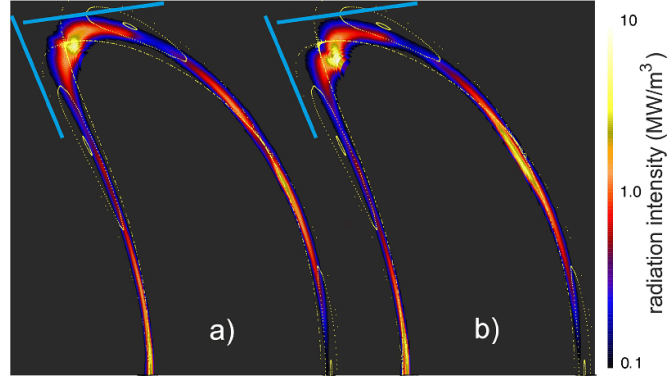


Figure 11. Radiation distributions for the standard island at (a) $f_{\text{rad}} = 0.8$, $n_{\text{IBS}} = 5.3 \times 10^{19} \text{ m}^{-3}$, and (b) $f_{\text{rad}} = 0.85$, $n_{\text{IBS}} = 5.4 \times 10^{19} \text{ m}^{-3}$.

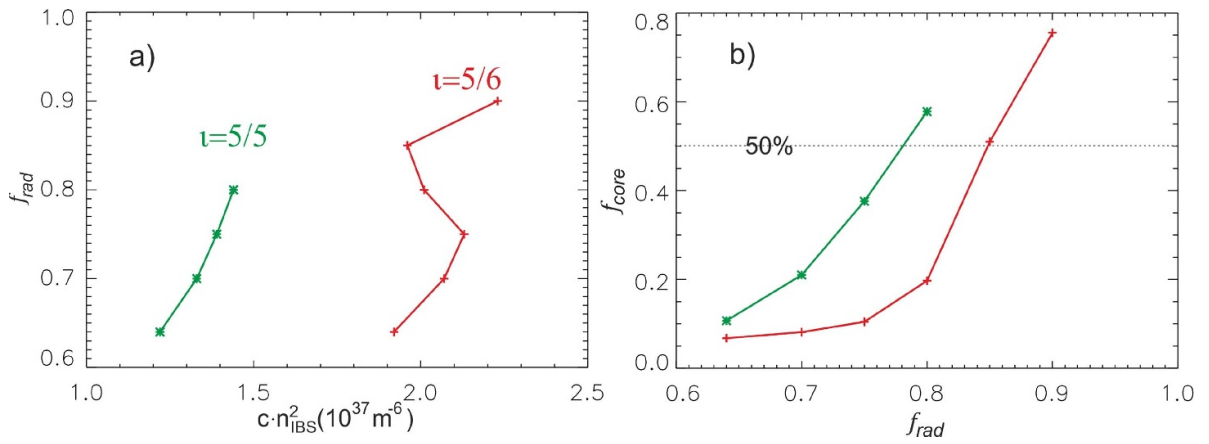


Figure 12. Same as figure 9, but with $\chi = 1.5 \text{ m}^2 \text{ s}^{-1}$ and without the high-iota island.

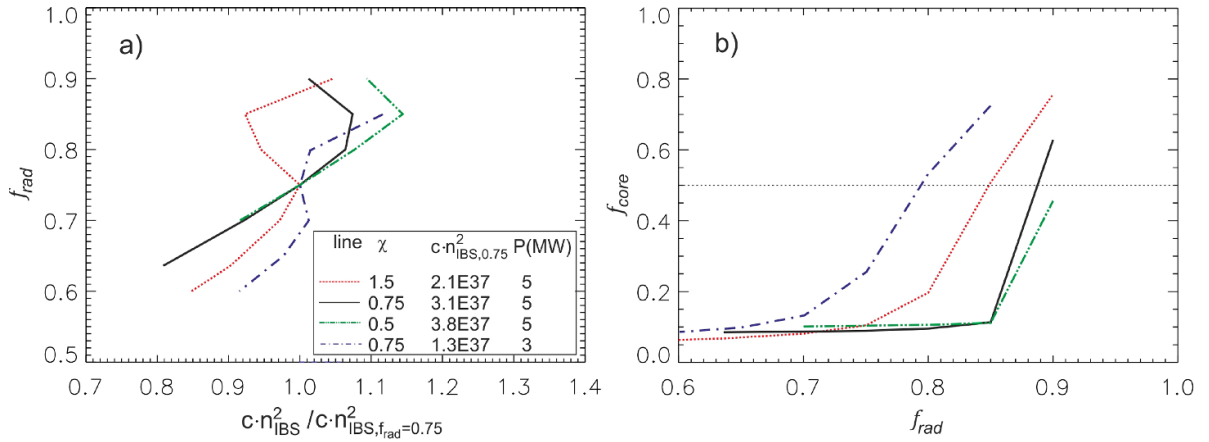


Figure 13. Sensitivity of the bifurcation to cross-field conductivity and power. (a) The radiation cost is normalized to its value at $f_{\text{rad}} = 0.75$, which is given in the figure legend. (a) The corresponding radiation fractions within the LCFS as a function of f_{rad} .

molecule-associated recombination should not play a significant role either, but this needs to be clarified in the future. On the other hand, the volume recombination processes (if any) take place closer to the target and should therefore have little effect on the radiation, which is close to the LCFS in the cases of interest here. To study the effects of the neutral gas on the radiation distribution and thereby on the detachment performance,

we conduct some numerical experiments in which we manipulate neutral baffles to control the neutral-plasma interaction.

For the low-iota divertor configuration, the main plasma-wall interaction (PWI) takes place at the horizontal target. The O-point is close to the horizontal target and the entire island is exposed to the recycling neutrals (see figures 5 and 7)—a situation that is quite different from the PWI of the standard island

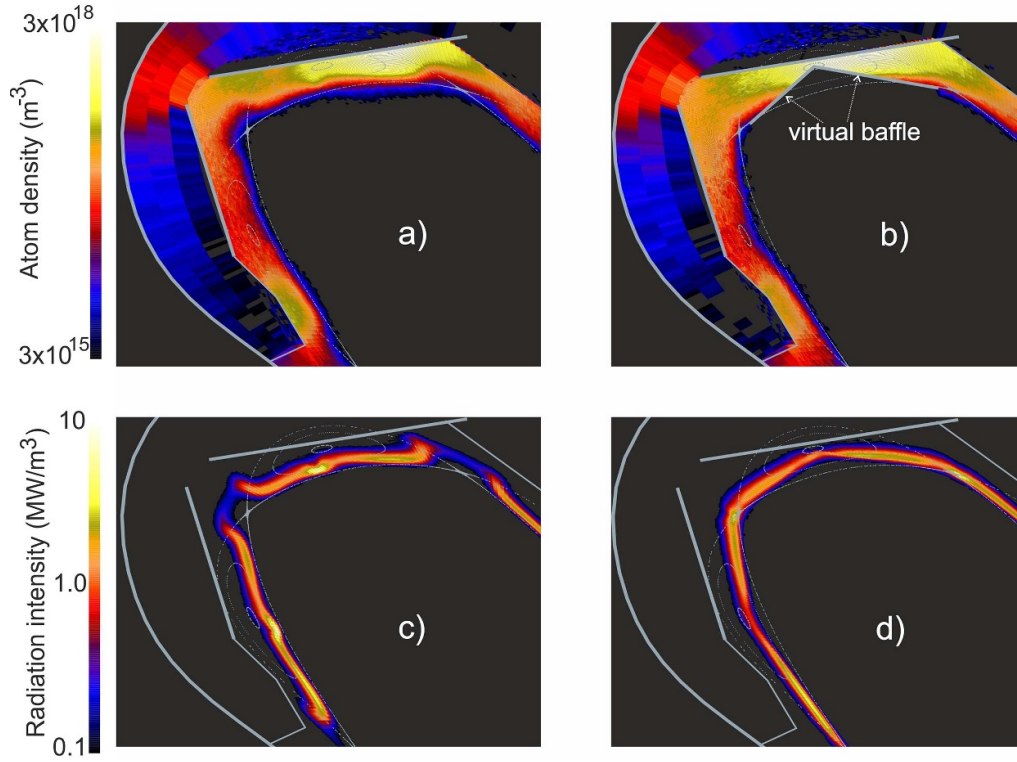


Figure 14. Distributions of hydrogen atoms in the low-iota island (*a*) without and (*b*) with the virtual baffle at $\phi = 10$ degrees (the toroidal center of the strike-line), and the corresponding radiation distributions. Input parameters are $P_{\text{SOL}} = 5$ MW, $f_{\text{rad}} = 0.85$, $n_{\text{IBS}} = 5.4 \times 10^{19} \text{ m}^{-3}$, $\chi = 0.5 \text{ m}^2 \text{ s}^{-1}$.

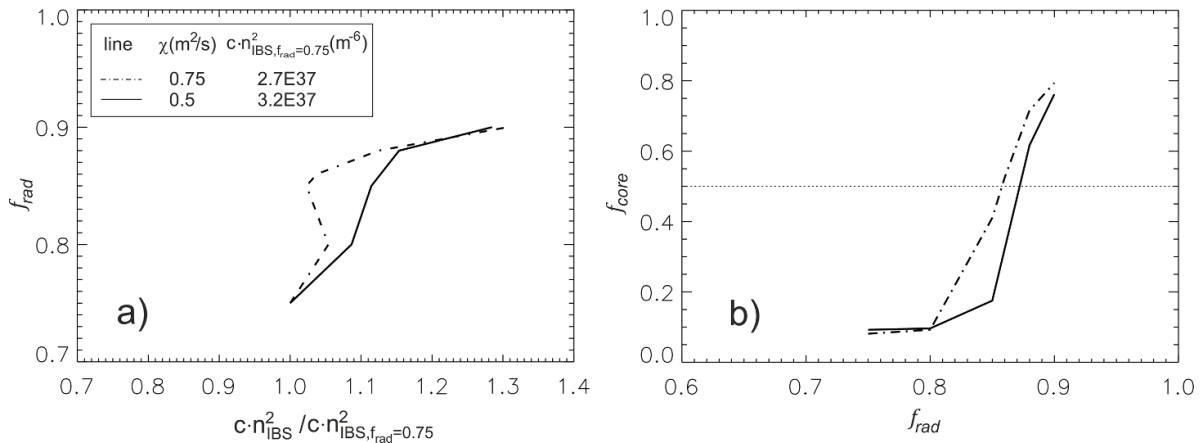


Figure 15. Same as the two cases with $\chi = 0.75$ and $0.5 \text{ m}^2 \text{ s}^{-1}$ at $P_{\text{SOL}} = 5$ MW in figure 13, but with the virtual baffle.

chain illustrated in figure 8, where the X-point is close to the strike-line on the horizontal target. To clarify the correlations of the impurity radiation distribution with the recycling neutrals, we introduce a virtual baffle below the horizontal target to prevent the neutral particles from directly entering the central area of the low-iota island. The virtual baffle is outlined in figure 14(b) and toroidally covers the entire PWI region. The word ‘virtual’ here means that this baffle can only act on the neutral particles and does not directly affect the background plasma but only indirectly through plasma-neutral interaction. In other words, the virtual baffle is a hypothetical surface that reflects neutral particles but is transparent to charged ones. The

resulting effects can be seen in figure 14, which compares the distributions of hydrogen atoms with and without the virtual baffle, and the consequences on the radiation distribution. The virtual baffle keeps the recycling neutrals out the island area where a radiation peak occurred below the horizontal target—figure 14(c). Consequently, this radiation peak and the one in front of the vertical target disappear, and the radiation starts to build up around the X-points.

The redistribution in radiation results in a change of the f_{rad} -behavior, as depicted in figure 15(a). Shown are the two simulation series with $\chi = 0.5$ and $0.75 \text{ m}^2 \text{ s}^{-1}$ at $P_{\text{SOL}} = 5$ MW. Compared to their earlier results without the virtual

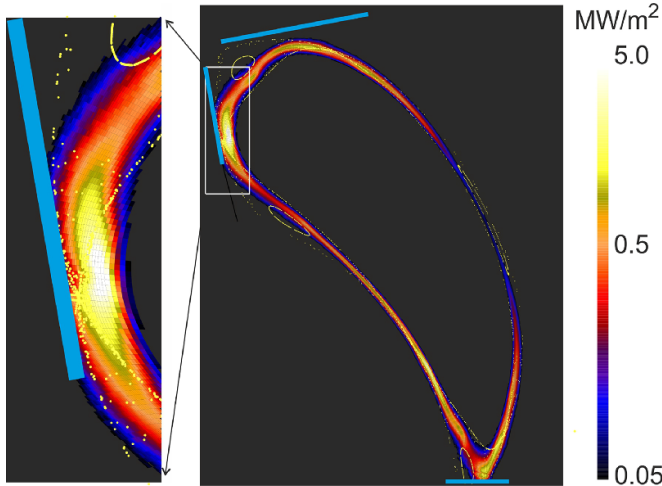


Figure 16. Radiation distribution at $\phi = 15$ degrees, where an X-point of the high-iota island is closest to the vertical target, taken from the simulation series shown in figure 9 at $f_{\text{rad}} = 0.64$.

baffle—figure 13(a)—the two f_{rad} -curves in figure 15(a) are smoother and the bifurcation disappears in the lower χ case. Also smoother are the f_{core} curves displayed in figure 15(b) compared to their partners in figure 13(b), indicating a smoother development of the radiation distribution during detachment when the recycling neutrals are deflected away from the central area of the island by the virtual baffle.

It can be concluded that the bifurcation is a combined effect of plasma-neutral interaction and a large ratio of perpendicular to parallel heat transport associated with the small field line pitch of the low-iota island—table 1. The recycling neutrals play a triggering role in the formation of O-point radiation, provided that the cross-field transport can transfer sufficient power there.

The reason for excluding the high-iota island from the comparative study in the previous section is also related to the recycling neutrals—a local PWI issue. It is found that an X-point of the high-iota island chain is too close to the vertical target to allow full development of the radiation layer in the island SOL. Figure 16 illustrates this situation with an enlarged image for the near-target region at the toroidal position where an X-point is closest to the vertical target. Unlike the other two islands, the high-iota island has much shorter connection lengths in the private flux region. The heat load there is visible on the IR-cameras, but not significant, which is consistent with the modeling results. The particle flux there is also low but appears to be strong enough to trigger intense radiation at the corresponding X-point already at $f_{\text{rad}} = 0.64$. For confirmation, dedicated simulations are carried out in which the vertical target is successively moved 2 and 5 cm away from the plasma and finally removed from the computational domain. For the high-iota island, the main PWI takes place at the so-called high-iota tail target (see in [36] for details), which is toroidally remote from the toroidal location under discussion. The manipulation of the vertical target does not alter the main PWI processes, but only the local one under discussion.

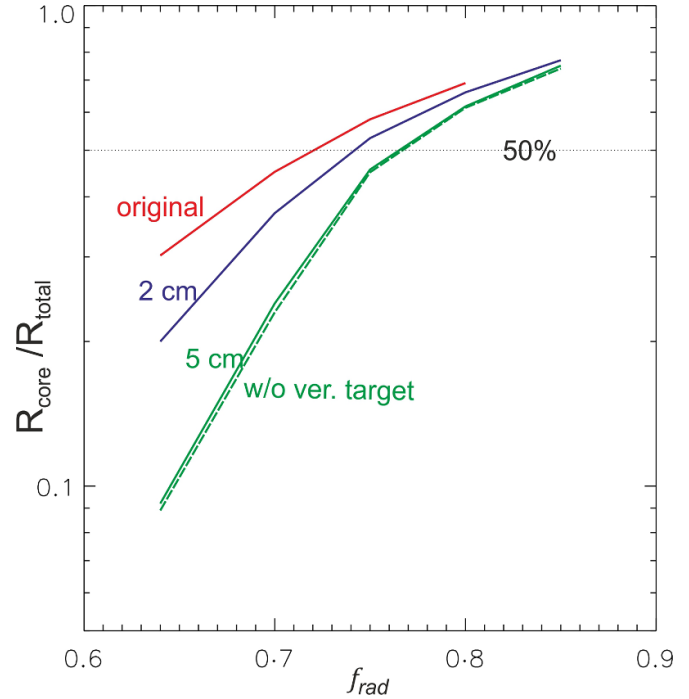


Figure 17. The proportion of radiation in the confinement region decreases when the vertical target is moved outwards until it is removed from the computation domain (dashed line).

The results are shown in figure 17. Moving the vertical target outward reduces the radiation fraction from the confinement region, especially in the low radiation range. As the total radiation increases, more and more radiation penetrates into the confinement region, and the effect induced by the vertical target becomes weaker and weaker. Retracting the vertical target by more than 5 centimeters does not yield more effects, as this distance already exceeds the typical width of the radiation layer.

In addition to the local PWI problem mentioned above, the 3D simulations indicate further potential to improve the overall PWI of the high-iota configuration to achieve better detachment performance. The high-iota configuration is attractive due to the larger island size and the greater field line pitch, especially as it produced the highest divertor neutral pressure measured to date [54]. Given the general importance of particle removal for the island divertor concept [55–57], a comprehensive numerical reassessment of the PWI for the high-iota island is in process.

4. Flux expansion effects

The 3D simulation results suggest that the radiation distribution around the X-point (XPR) favors detachment due to the lower radiation costs. The separation of the magnetic surfaces around the X-point is greater than that between the neighboring X-points. This is referred to as flux expansion. In the following, we present simpler models to explain why and how flux expansion enhances radiation, and thus favoring

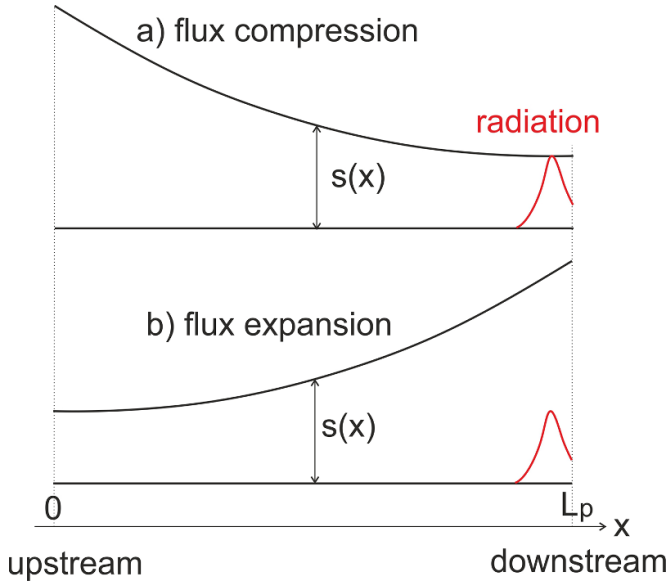


Figure 18. Schematic of two flux tubes with varying height of $s(x)$. The downstream position is defined at the right end. The flux tube (a) is compressed downstream, while (b) (a mirror image of (a)) is expanded. The red curves indicate the location of impurity radiation, which is specified by setting $T_e = 2$ eV at $x = L_p$.

detachment. The purpose is to illustrate the basics, not to attempt to match the 3D results.

4.1. Analytical, 1D and quasi-2D models

First, we reduce the dimensionality from 3D to 2D and use the island geometry described in section 2. After this approximation, the 3D information of the helical island and the associated radiation distribution are lost, but the basic feature is retained, namely that the flux surfaces are expanded in the region near the X-point and compressed in the area between the neighboring X-points (see figure 1), regardless of the actual location of the island. We focus only on the principles, not on the absolute numbers. With this in mind, we consider here a flux tube that is formed by two adjacent flux surfaces, one of which is the separatrix and the other lies within the LCFS. The spacing between the two surfaces varies with $\Delta\theta$ according to equation (3), and has a maximum at $\Delta\theta = 0$ or 2π and a minimum at $\Delta\theta = \pi$. Due to the left-right mirror symmetry of the 2D magnetic island, we only consider half of the island with $\Delta\theta$ between 0 and π . Figure 18(a) illustrates the flux tube where $\Delta\theta$ is represented by the poloidal length of $x = L_p \cdot \Delta\theta/\pi$ with $L_p = W_p/2$. We introduce a flux expansion factor, defined as $f_{ep} = s_{rad}/s_a$, where s_{rad} is the s value at the radiation location x_{rad} , and s_a is its average value given by $s_a = \int s \cdot dx/L_p$. We refer to f_{ep} here as the flux expansion factor, although f_{ep} can be less than unity when $s_{rad} < s_a$. Neglecting the spatial variation of B, magnetic flux conservation means that $s \cdot \Theta = \text{constant} = s_a \cdot \Theta_a$ with Θ_a being the average field line pitch. Then, the field line pitch Θ varies with s as $\Theta = s_a \cdot \Theta_a/s$. Thus, the flux expansion factor describes

the extent to which the local field line pitch at the location of impurity radiation differs from its mean value.

Flux expansion effects can be studied by varying x_{rad} between 0 and L_p . However, for numerical convenience, we use a different but equivalent strategy here: we fix the radiation at the downstream position defined at the right end of the flux tube, i.e. we set $x_{rad} = L_p$, and vary s_{down} there, and thereby the flux expansion factor $f_{ep} = s_{down}/s_a$, while keeping s_a unchanged. This is achieved by changing the ratio of $\Delta r_0/r_1$ in equation (3) under the constraint of $s_a = \int s \cdot dx/L_p$. Equation (3) can only generate cases of $f_{ep} < 1$, and the cases where $f_{ep} > 1$ are then obtained by inverting the x -coordinates, as indicated in figure 18(b). In this way, f_{ep} can be varied gradually over a range of interest.

In the following, we present three models in order to demonstrate different physical effects. We assume pressure conservation along the magnetic field, i.e.

$$p_e = nT_e = \text{constant}. \quad (5)$$

Without detailed derivation, equation (5) and the radiation function—equation (4) - already imply an interesting effect. L_z has a maximum at a certain T_e point. Let us consider a local plasma in which T_e is somewhere above the point of the maximum L_z . Once T_e drops due to impurity radiation, L_z increases and the plasma density also rises due to the pressure conservation. Both strengthen the impurity radiation and thereby lower T_e further until T_e falls to a level at which L_z has decreased significantly (see figure 6). Finally, a cold, dense plasma forms locally, called plasma condensation. The strongly localized radiation shown by the 3D simulations actually reflects the plasma condensation effect, although the plasma pressure is not strictly constant along the field lines.

Model I. We start with the following heat transport model that only takes into account heat conduction processes, i.e.

$$q_x = - \left(\Theta^2 \kappa_e T_e^{5/2} + 2\chi n \right) \frac{dT_e}{dx}. \quad (6)$$

The heat flux density q_x consists of contributions of the parallel electron heat conduction and the perpendicular heat fluxes of electrons and ions with the same temperature and conductivity χ . For simplicity, χ is assumed to be independent of plasma temperature. Impurity radiation is based on equation (4) and uses the cooling rate Cr^a in figure 6. There is no volume heat source. Instead, $q_x = P_{in}/s$ is given at $x=0$ with $P_{in} = P_{SOL}/(4\pi mR)$, where m is the poloidal mode number of the magnetic island and R is the major radius. Model I reads

$$\frac{1}{s} \frac{d}{dx} (s \cdot q_x) = -c \cdot n^2 \cdot L_z(T_e) \quad (7)$$

where the pressure constant is determined by equalizing the total impurity radiation P_{rad} with P_{in} , i.e. 100% radiation.

This simple model allows an analytical analysis to show a radiation volume effect. Defining $Q_x = s \cdot q_x$ and using equation (6), we can transform equation (7) to T_e -space as

$$\frac{d}{dT_e} Q_x^2 = 2c \cdot s^2 n^2 \left(\Theta^2 \kappa_e T_e^{5/2} + 2\chi n \right) \cdot L_z(T_e). \quad (8)$$

Integrating equation (8) from T_{down} to T_{up} yields

$$\begin{aligned} Q_{x,\text{up}}^2 = P_{\text{in}}^2 = 2c(s \cdot \Theta)^2 p_e^2 & \left(\kappa_e \int_{T_{\text{down}}}^{T_{\text{up}}} L_z(T_e) T_e^{1/2} dT_e \right. \\ & \left. + 2\chi p_e \int_{T_{\text{down}}}^{T_{\text{up}}} \frac{L_z(T_e)}{\Theta^2 T_e^3} dT_e \right) \end{aligned} \quad (9)$$

where equation (5) has been used. The first term in the parentheses is associated with the parallel heat transport, and the second term with the cross-field heat conduction. The latter becomes increasingly important as Θ decreases. In the range of Θ and plasma parameters of interest in this work, the parallel heat flux is much larger than the perpendicular one in the region outside the radiation zone, while it drastically decreases in the radiation zone due to the low temperature and high plasma density. For carbon, the first term on the right side of equation (9) is much smaller than the second one, especially under the conditions of flux expansion. As the radiation is localized downstream and distributed in a small x -range in which Θ does not change much, we assume $\Theta = \Theta_{\text{down}}$, extract it from the second integral, and denote the remaining integral by R_{\perp} . Ignoring the first term contributed by the parallel heat conduction, equation (9) reduces to

$$P_{\text{rad}} = Q_{x,\text{up}} = 2\sqrt{c\chi p_e^3 R_{\perp}} \cdot s_a \cdot f_{\text{ep}} \quad (10)$$

where $f_{\text{ep}} = s_{\text{down}}/s_a = \Theta_a/\Theta_{\text{down}}$. Equation (10) shows that the total radiation scales linearly with the flux expansion factor f_{ep} , which means that under otherwise identical conditions, plasma condensation at the point where the flux surfaces are expanded leads to more radiation—a radiation volume effect. In contrast, the contribution of parallel transport—the first integral in equation (9) - does not benefit from this flux expansion effect.

Model II. In fact, plasma condensation is not purely a 1D problem as discussed above, but at least a 2D question. Even if the radiation can be restricted to a flux tube of limited width, the strong variation of the plasma parameters inside the flux tube will affect the surrounding plasma. In the following, we will make some approximations for the interaction with the surrounding plasma rather than performing a strict 2D treatment. We first assume that the heat comes from the flux surface in contact with the hot plasma side by conduction and convection processes, i.e. $-2\chi n \cdot dT_e/dr$ and $-5T_e D \cdot dn/dr$, where $T_i = T_e$ has been assumed. The consideration of the convective heat flow has already implied a particle flux into or out of the hot plasma side, which will be discussed later. For simplicity, we assume $\chi = 2.5D$ ($D = \text{diffusivity}$), so that the conductive and convective heat fluxes are combined into one term driven by p_e -gradient, i.e. $-(2\chi n \cdot dT_e/dr + 5T_e D \cdot dn/dr) = -2\chi \cdot dp_e/dr$. We still assume spatially constant cross-field transport coefficients, and approximate $-dp_e/dr$ by $(p_{e0} - p_e)/s$,

where p_{e0} is the electron thermal pressure on the adjacent high-temperature surfaces, which are assumed to be isothermal. Adding this local heat source to equation (7), we have

$$\frac{1}{s} \frac{d}{dx} (s \cdot q_x) = -c \cdot n^2 \cdot L_z(T_e) + 2\chi \frac{p_{e0} - p_e}{s^2}. \quad (11)$$

Here, p_{e0} can be regarded as a regulation parameter that ensures that the integrated volume heat source is equal to P_{in} . In short, model II addresses heat source effects.

Model III. The next step is to add convective heat fluxes to equation (11), which requires the inclusion of particle balance (continuity). The equations addressed in model III are

$$\frac{1}{s} \frac{d}{dx} s \cdot (q_x + 5T_e \Gamma_x) = -c \cdot n^2 \cdot L_z(T_e) + 2\chi \frac{p_{e0} - p_e}{s^2} \quad (12)$$

$$\frac{1}{s} \frac{d}{dx} (s \cdot \Gamma_x) = D \frac{n_a - n}{s^2} \quad (13)$$

where $\Gamma_x = \Theta n u_{\parallel} - D \cdot dn/dx$ and includes the parallel and perpendicular particle fluxes, and u_{\parallel} is the parallel plasma flow velocity, which vanishes at $x = 0$ and $x = L_p$ due to the symmetry of the magnetic island under discussion. In analogy with the heat source term in equation (11), the right-hand side in equation (13) is the particle source due to diffusion into or out of the hot-plasma side, as mentioned earlier, where the density is assumed be constant and equal to n_a . Equation (13) does not take into account the ionization sources of recycling neutrals, so the right-hand term does not model any net particle source, but only the diffusive particle flux across the field.

In the radiation zone, the plasma density is higher than n_a so that electrons and ions can escape from the flux tube into the hot plasma side by diffusion. These escaping particles return to the flux tube at the upstream positions where n is lower than n_a , and then flow back to the radiation zone along the magnetic field, thus closing the streamlines of the flow. The resulting convective heat flux reduces the conductive one, and thus the related parallel temperature gradient. Model III contains a further effect, namely that the escaping particle flux is lower where the magnetic surfaces are rather apart (i.e. in regions of large flux expansion), thus favoring a build-up of plasma density.

Integrating the right-hand term of equation (13) and setting the integral to be zero, we get

$$n_a = \int_0^{L_p} dx \cdot (n/s) / \int_0^{L_p} dx/s. \quad (14)$$

It is not surprising that n_a appears as the average plasma density in the flux tube, since in the absence of an ionization source, all closed flux tubes must have the same average density of n_a . Hence, equation (14) also applies to the evaluation of the average plasma density for models I and II, although continuity is not explicitly included in them.

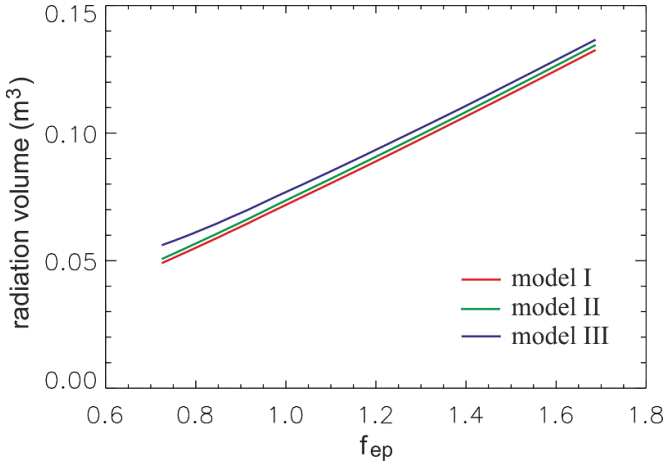


Figure 19. Radiation volume increases linearly with f_{ep} . It is assumed that $s_a = 3$ cm.

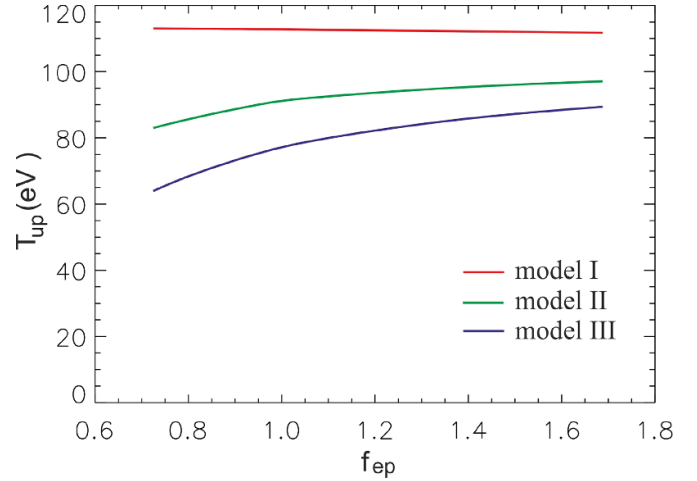


Figure 20. Upstream temperature as a function of f_{ep} resulting from different models.

4.2. Model results

The following analysis uses the standard magnetic island of W7-X as a reference. The shape of the flux tube follows equation (3) and different f_{ep} values are obtained by varying the ratio of $\Delta r_0/r_i$ while keeping s_a unchanged. Hydrogen plasma is assumed with 1% impurity concentration, $P_{SOL} = 5$ MW, $D = 0.4 \text{ m}^2 \text{ s}^{-1}$, and $\chi = 1 \text{ m}^2 \text{ s}^{-1}$. Figure 19 displays the radiation volume as a function of f_{ep} calculated using the three models. The radiation volume is evaluated by dividing P_{SOL} with the peak radiation intensity. Here, the scaling of the radiation volume is more meaningful than the absolute numbers, since the latter depend on the assumed s_a .

All three models show a linear relationship between the radiation volume and f_{ep} , as expected from the analytical model—equation (10). The good agreement in the f_{ep} scaling of the radiation volume is due to the highly localized radiation. The models differ only in the transport processes, which take place mainly on the way to, but outside of, the radiation zone.

Differences between the models are evident in the upstream temperature determined at $x=0$, as can be seen in figure 20. Switching from the given upstream heat flux in model I to the x -dependent heat source in model II leads to an overall drop in the upstream temperature due to the reduced heat flux over most of the path to the radiation zone. The stronger decrease of T_{up} in the low f_{ep} range is due to the fact that some of the energy source is located further downstream because of the s -dependence of the local source in equation (11). The convective heat flux included in model III further lowers T_{up} because of the reduced heat flux in the conduction channel driven by T_e -gradient. Thus, as f_{ep} is increased, the continuous increase of T_{up} in models II and III is attributed to the gradual relocation of the heat source from downstream toward upstream as the flux surfaces become more expanded downstream and more compressed upstream.

Another important plasma parameter is the average density n_a , which not only controls the plasma density but also, within the context of the concentration model, the impurity

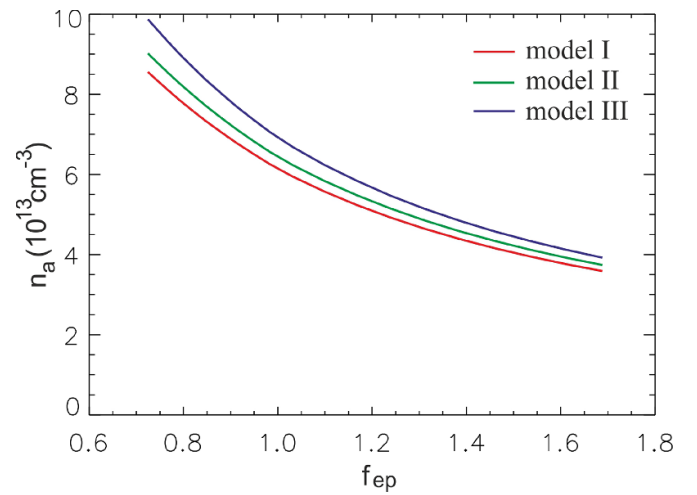


Figure 21. Average plasma density as a function of f_{ep} from Model I, II, and III.

density on the side of the confinement region where the heat comes from, and thus the corresponding particle content. A change in n_a will not be a purely local effect in the flux tube under discussion, but has an impact on the surrounding confinement region. Figure 21 displays the f_{ep} -dependence of n_a from the three models. All three models show a continuous drop in n_a as f_{ep} increases. The decrease in n_a cannot be entirely attributed to the radiation volume effect—equation (10) and figure 19. It is generally true that a larger radiation volume in a flux expansion area, for a fixed impurity concentration, lowers the plasma density in the radiation zone required to remove a given power. The plasma density weighted by the radiation intensity indeed decreases with f_{ep} , but only by a factor about 1.4 over the relevant f_{ep} range evaluated by the most realistic model III, which is much weaker than the changes of n_a shown in figure 21. This is because n_a represents an average density weighted by $1/s$ —equation (14). Physically, this can be explained in that the density build-up at the place where magnetic flux surfaces expand has a smaller effect on the

plasma density in the confinement region. The high sensitivity of n_a to f_{ep} shown in figure 21 demonstrates the importance of flux expansion in reducing the plasma density required for detachment.

5. The necessary condition for XPR

The prerequisite for the XPR is that the classical electron heat conduction must be able to conduct most of the power to the region near the X-point, which is controlled by the divertor-relevant poloidal field component $b_p = (r_a/R) \cdot (\iota - n/m)$. In contrast, the radial field component b_r does not transfer heat in the poloidal direction, but only slightly bends the poloidal heat channel into the radial direction. Cross-field transport creates a bypass that competes with this poloidal heat flux. Regarding XPR, the often-mentioned ‘parallel to perpendicular transport ratio’ actually refers to the ratio between this poloidal heat flux and the radial heat flux from cross-field transport. In the following, we estimate this ratio based on the characteristics of parallel and perpendicular transport scale lengths.

We denote the poloidal and radial directions by x and y respectively and neglect the curvature of the flux surfaces around the rational surface in the limit of small r_i/r_a . The poloidal heat flux mostly comes from parallel heat conduction, whereas the radial heat flux originates from cross-field transport. Together, they must satisfy the heat transport equation

$$\frac{d}{dx} \left(-b_p^2 \kappa_e T_e^{5/2} \frac{dT_e}{dx} \right) + \frac{d}{dy} \left(-2\chi \frac{d(nT_e)}{dy} \right) = 0 \quad (15)$$

where the cross-field transport (second term) again consists of both conduction and convection, as argued in equation (11). The poloidal transport length is fixed by the poloidal width of the island, i.e. $L_p = W_p/2$. We introduce a power decay length λ_p to characterize the radial transport scale length. To make the discussion easier, the heat transport can be thought of as taking place in a box, with x ranging from 0 to L_p and y from 0 to λ_p . In equation (15), the power loss due to neutral gas is neglected and the impurity radiation is represented by a surface energy sink at $x = L_p$. Under the assumption of pressure conservation along x , equation (15) can be approximated as

$$\lambda_p \cdot \frac{d}{dx} \left(-b_p^2 \kappa_e T_e^{5/2} \frac{dT_e}{dx} \right) = q_{\perp} - 2\chi \frac{p_e}{\lambda_p} \quad (16)$$

where q_{\perp} is the perpendicular heat flux density on the hot-plasma side, i.e. at $y = 0$, and the second term on the right hand side is the heat flux escaping from the box at $y = \lambda_p$ due to the cross-field transport. We define the upstream position at $x = 0$, where $T_e = T_{up}$ and the poloidal heat flux is zero. Integrating equation (16), we get

$$-\frac{2}{7} \lambda_p b_p^2 \kappa_e \frac{dT_e^{7/2}}{dx} = \left(q_{\perp} - 2\chi \frac{p_e}{\lambda_p} \right) x. \quad (17)$$

Downstream is located at $x = L_p$, where $T_e = T_{down} \ll T_{up}$. Using $p_e = T_{up} n_{up}$, integrating equation (17) from $x = 0$ to $x = L_p$ yields

$$\frac{4}{7} b_p^2 \kappa_e T_{up}^{7/2} \frac{\lambda_p}{L_p} + 2\chi n_{up} T_{up} \frac{L_p}{\lambda_p} = q_{\perp} L_p. \quad (18)$$

The right side is the total power into the heat transport box. The first term on the left side is the power transferred downstream through the parallel conduction channel and the second is the power that escapes from the box through the cross-field transport channel. If we define a critical value of λ_p as λ_c , at which the two fluxes are equal, then λ_c is given by

$$\lambda_c = \left(\frac{28}{\kappa_e} \right)^{2/9} \frac{(\chi n_{up})^{7/9}}{q_{\perp}^{5/9}} \left(\frac{W_p}{b_p} \right)^{4/9} \quad (19)$$

where $L_p = W_p/2$ has been used. In fact, λ_c defines the characteristic radial width of the parallel power channel. It is obvious that the power channel must be narrower than half the radial width of the island. Without further justification, we define $\lambda_c < r_i = W_r/2$ as the necessary condition for the parallel transport to transfer most of the power into the near-X-point region. To meet this requirement, the magnetic island must satisfy the condition of

$$r_i \cdot b_{rm}^{4/5} > \pi^{4/5} \left(\frac{7}{\kappa_e} \right)^{2/5} \frac{(\chi n_{up})^{7/5}}{q_{\perp}} \quad (20)$$

where b_p is replaced by b_{pm} and the relation of $b_{pm}/b_{rm} = 4/\pi \cdot W_p/W_r$ has been used [47]. Using $L_{co} = \pi \cdot r_i/b_{rm}$ (the field line length to complete an internal poloidal turn at the O-point [47]) as a characteristic connection length of the magnetic island, equation (20) can be rewritten as

$$W_r/L_{co}^{4/9} > 2 \left(\frac{7}{\kappa_e} \right)^{2/9} \frac{(\chi n_{up})^{7/9}}{q_{\perp}^{5/9}}. \quad (21)$$

Conditions (20) and (21) relate the island geometry on the left side to the plasma parameters on the right side. It is not yet clear how the heat conductivity χ at the plasma edge depends on the edge plasma density and the heating power in W7-X. If χ would decrease with the plasma density and increase with the heating power, as expected based on the ISS95 [58] and ISS04 [59] databases or the local scaling of W7-AS [60], then conditions (20) and (21) would not be as sensitive to the edge plasma density and heating power as they appear to be. In particular, if the local scaling of W7-AS [60] would also apply to W7-X, the three plasma parameters on the right-hand side of conditions (20) and (21) would almost cancel each other out. Roughly speaking, the above conditions show that larger islands and stronger perturbation fields or shorter connection lengths favor the formation of XPR and the associated detachment stability, which qualitatively agrees with the experimentally observed trends in W7-X [33, 35, 43].

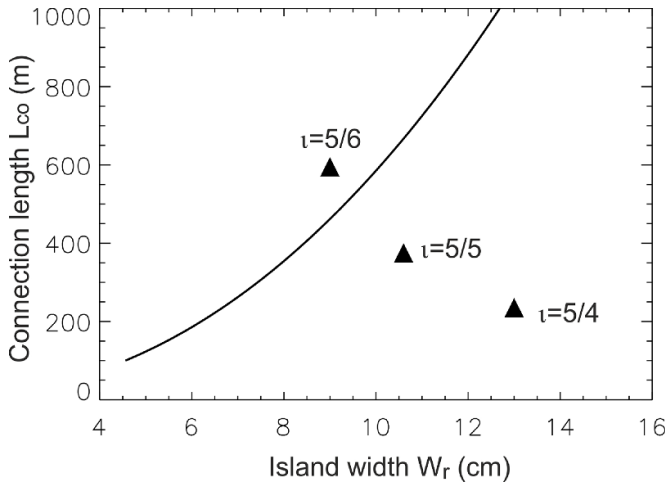


Figure 22. Diagram of island size and connection length for X-point radiation. The solid curve is the $W_r - L_{co}$ scaling expected by equation (21) with $\chi = 0.75 \text{ m}^2 \text{ s}^{-1}$, $n_{up} = 5 \times 10^{19} \text{ m}^{-3}$ and $P_{SOL} = 5 \text{ MW}$. The lower right area favors X-point radiation. The triangular symbols indicate the location of the three island chains according to their geometric parameters given in table 1.

The actual geometry of the target is not explicitly included in the derivation of conditions (20) and (21), but is to some extent implied by the assumption that $\lambda_c < r_i$. In fact, the current W7-X divertor was designed so that the targets intersect the three studied island chains approximately through their O-points. With this constraint, it should be possible to establish a correlation between L_{co} and the target-to-target connection length, as the latter is easier to estimate in practice. However, the W7-X island divertor has a high degree of configuration flexibility, and the target-to-target connection length is not an explicitly decisive parameter for the parallel-to-perpendicular heat transport ratio. In addition, it is important to note that a significant deviation of the PWI situation from the design scenario can lead to effects that are not covered in this paper, such as those numerically investigated in [34].

The quantitative significance of conditions (20) or (21) need to be assessed by comprehensive experimental validation. As a starting point, we apply it to the 3D modeling results of the three island chains. Figure 22 shows the $W_r - L_{co}$ scaling predicted by condition (21) with $\chi = 0.75 \text{ m}^2 \text{ s}^{-1}$, $n_{up} = 5 \times 10^{19} \text{ m}^{-3}$ and $P_{SOL} = 5 \text{ MW}$, which are the standard setting in the island scan in section 3. Depicted are also the three vacuum island chains based on table 1. Magnetic islands in the lower right area of the $W_r - L_{co}$ curve favor XPR. Interestingly, the low-iota island does appear to be slightly above the $W_r - L_{co}$ curve, while the other two islands are below it. Considering finite beta effects, it is expected that the actual $\iota = 5/6$ island is smaller and therefore lies further to the left, whereas the standard island is actually larger and lies further to the right.

Condition (21) is a necessary but not sufficient condition for XPR, for which careful control of the recycling neutrals is crucial.

6. Conclusions

With the help of the VMEC code, we geometrically characterized the three island chains in the divertor configuration space of W7-X, compared their behavior under detached conditions using the EMC3-Eirene code, and explained the physics behind the main 3D results with simpler models.

Using the EMC3-Eirene code, we scanned the three island chains under otherwise identical code settings and found that they behave differently in the radiation distribution and the evolution of the radiation zone during the detachment phase. While the radiation increases in the detachment phase, the standard magnetic island chain, which is the most studied divertor configuration so far about detachment, has typically shown that intense radiation first occurs near the strike line at the target, then moves inward to the X-point, and finally enters the confinement area through the X-point—the so-called ‘XPR’. In contrast, the low-iota island chain features a radiation distribution that concentrates in the interior of the magnetic island between the neighboring X-points, referred to here as ‘O-point radiation’. However, once the radiation front enters the confinement region of the low-iota configuration at higher radiation levels, the radiation begins to build up around the X-point and form a radiation pattern similar to the XPR of the standard island. The radiation distribution is directly related to the radiation costs, which in this work are defined as the product of the plasma and impurity densities on a closed flux surface about eight centimeters inside the LCFS. While the radiation costs for the standard island chain increase linearly with the total radiation throughout the investigated detachment phase, the low-iota island chain shows a bifurcation behavior in that the radiation costs initially increase with the radiation and then decrease when the radiation distribution changes from the O- to the XPR pattern. Consistent with the numerical results, the detachment experimentally achieved with the standard island is stable [35, 43, 44], whereas unstable with the low-iota island chain [33]. For the high-iota island chain, a local PWI issue was identified that severely limits its actual performance under detached conditions, which will be verified in the upcoming experimental campaign period.

With the help of simpler models, we have clarified why XPR can reduce the radiation costs. The flux expansion in the area of the X-point further reduces the already small field-line pitch of the island divertor and thus increases the weight of the cross-field heat conduction in the radiation zone. 1D analyses have shown that the cross-field heat transport plays the predominant role in the radiation zone and increases the radiation volume at the location where the flux surfaces are expanded. In addition, the build-up of plasma and impurity density in the area of flux expansion has weaker effects on the surrounding plasma in the confinement region. All these factors reduce the plasma and impurity density required to radiate a given amount of power at detachment. However, the prerequisite for achieving XPR is that the magnetic island and the field line pitch must be large enough to allow the electrons

to conduct most of the power to the near X-point area, which has been estimated analytically and found to be a function of the size of the magnetic island, the connection length, the cross-field heat conductivity, the power flux as well as the edge plasma density. This analytical result is in good qualitative agreement with the experimental observations of W7-X and even shows a certain quantitative relevance for the three island chains discussed in this paper, which, however, still requires further extensive experimental validation. The condition that most of the power must be transferred to the X-point region is necessary but not sufficient to achieve XPR, as the recycling neutrals can alter the radiation distribution through the associated ionization sources and energy sinks. The O-point radiation produced by EMC3-Eirene for the low-iota island, which has been predicted in [33] and is confirmed in this work, is understood to be a combined effect of the small field line pitch and an 'unfavorable' situation of plasma-neutral interaction. As the radiation layer enters the confinement region, the field line pitch increases (see figure 1), leading to a relocation of radiation from the O-point to the X-point. Due to the flux expansion effect mentioned above, this redistribution of radiation is not a monotonic process but leads to a bifurcation in the radiation costs, i.e. a further increase in the total radiation requires a reduction in the plasma or impurity density, or both.

Acknowledgments

This work has been carried out within the framework of the EUROfusion Consortium, funded by the European Union via the Euratom Research and Training Programme (Grant Agreement No 101052200 - EUROfusion). Views and opinions expressed are however those of the author(s) only and do not necessarily reflect those of the European Union or the European Commission. Neither the European Union nor the European Commission can be held responsible for them. The corresponding author would like to thank Drs Tilmann Lunt, Ou Pan, Matthias Bernert for their enlightening discussions on XPR in ASDEX-Upgrade.

ORCID iDs

Y. Feng  <https://orcid.org/0000-0002-3846-4279>
 V. Winters  <https://orcid.org/0000-0001-8108-7774>
 D. Zhang  <https://orcid.org/0000-0002-5800-4907>
 J. Geiger  <https://orcid.org/0000-0003-4268-7480>
 Y. Gao  <https://orcid.org/0000-0001-8576-0970>
 P. Helander  <https://orcid.org/0000-0002-0460-590X>
 C.D. Beidler  <https://orcid.org/0000-0002-4395-239X>
 M. Endler  <https://orcid.org/0000-0003-2314-8393>
 M. Jakubowski  <https://orcid.org/0000-0002-6557-3497>
 T. Kremeyer  <https://orcid.org/0000-0002-6383-944X>
 V. Perseo  <https://orcid.org/0000-0001-8473-9002>
 G. Schlisio  <https://orcid.org/0000-0002-5430-0645>

References

- [1] Klinger T. *et al* 2019 Overview of first Wendelstein 7-X high-performance operation *Nucl. Fusion* **59** 112004
- [2] Wolf R. *et al* 2017 Major results from the first plasma campaign of the Wendelstein 7-X stellarator *Nucl. Fusion* **57** 102020
- [3] Dinklage A. *et al* 2018 Magnetic configuration effects on the Wendelstein 7-X stellarator *Nat. Phys.* **14** 855
- [4] Pedersen T.S. *et al* 2022 Experimental confirmation of efficient island divertor operation and successful neoclassical transport optimization in Wendelstein 7-X *Nucl. Fusion* **62** 042022
- [5] Beidler C. *et al* 2021 Demonstration of reduced neoclassical energy transport in Wendelstein 7-X *Nature* **596** 221
- [6] Helander P. 2014 Theory of plasma confinement in non-axisymmetric magnetic fields *Rep. Prog. Phys.* **77** 087001
- [7] Wobig H. 1993 The theoretical basis of a drift-optimized stellarator reactor *Plasma Phys. Control. Fusion* **35** 903
- [8] Nührenberg J. 2010 Development of quasi-isodynamic stellarators *Plasma Phys. Control. Fusion* **52** 124003
- [9] Renner H., Boscary J., Greuner H., Grote H., Hoffmann F.W., Kisslinger J., Strumberger E. and Mendelevitch B. 2002 Divertor concept for the W7-X stellarator and mode of operation *Plasma Phys. Control. Fusion* **44** 1005
- [10] Wagner F. *et al* 2005 W7-AS: one step of the Wendelstein stellarator line *Phys. Plasmas* **12** 072509
- [11] Hirsch M. *et al* 2008 Major results from the stellarator Wendelstein 7-AS *Plasma Phys. Control. Fusion* **50** 053001
- [12] McCormick K. *et al* 2002 New advanced operational regime on the W7-AS stellarator *Phys. Rev. Lett.* **89** 015001
- [13] Grigull P. *et al* 2001 First island divertor experiments on the W7-AS stellarator *Plasma Phys. Control. Fusion* **43** A175
- [14] König R. *et al* 2002 The divertor program in stellarators *Plasma Phys. Control. Fusion* **44** 2365
- [15] Iiyoshi A. *et al* 1999 Overview of the large helical device project *Nucl. Fusion* **39** 1245
- [16] Ohya N. *et al* 1994 The large helical device (LHD) helical divertor *Nucl. Fusion* **34** 387
- [17] Kobayashi M. *et al* 2010 Transport characteristics in the stochastic magnetic boundary of LHD: magnetic field topology and its impact on divertor physics and impurity transport *Fusion Sci. Technol.* **58** 220
- [18] Feng Y. *et al* 2008 Fluid features of the stochastic layer transport in LHD *Nucl. Fusion* **48** 024012
- [19] Kobayashi M. *et al* 2007 Divertor transport study in the large helical device *J. Nucl. Mater.* **363** 294
- [20] Kobayashi M. *et al* 2013 Edge impurity transport study in the stochastic layer of LHD and the scrape-off layer of HL-2A *Nucl. Fusion* **53** 033011
- [21] Feng Y. *et al* 2009 Comparative divertor-transport study for helical devices *Nucl. Fusion* **49** 095002
- [22] Feng Y., Kobayashi M., Lunt T. and Reiter D. 2011 Comparison between stellarator and tokamak divertor transport *Plasma Phys. Control. Fusion* **53** 024009
- [23] Boozer A.H. 2015 Stellarator design *J. Plasma Phys.* **81** 515810606
- [24] Bader A., Boozer A.H., Hegna C.C., Lazerson S.A. and Schmitt J.C. 2017 HSX as an example of a resilient non-resonant divertor *Phys. Plasmas* **24** 032506
- [25] Janeschitz G. *et al* 1992 Divertor performance on carbon and beryllium targets in JET *J. Nucl. Mater.* **196** 380
- [26] Petrie T. *et al* 1992 Divertor heat flux reduction by D2 injection in DIII-D *J. Nucl. Mater.* **196** 848
- [27] Krasheninnikov S. and Kukushkin A. 2017 Physics of ultimate detachment of a tokamak divertor plasma *J. Plasma Phys.* **83** 155830501

- [28] Stangeby P. 2018 Basic physical processes and reduced models for plasma detachment *Plasma Phys. Control. Fusion* **60** 044022
- [29] Grigull P. *et al* 2003 Divertor operation in stellarators: results from W7-AS and implications for future devices *Fusion Eng. Des.* **66** 49
- [30] Feng Y. *et al* 2005 Physics of the geometry-related detachment stability in W7-AS *Nucl. Fusion* **45** 89
- [31] Kobayashi M. *et al* 2013 Control of 3D edge radiation structure with resonant magnetic perturbation fields applied to the stochastic layer and stabilization of radiative divertor plasma in LHD *Nucl. Fusion* **53** 093032
- [32] Kobayashi M. and Tokar M. 2019 Experimental studies of and theoretical models for detachment in helical fusion devices *Fusion Energy* (IntechOpen) p 55
- [33] Winters V.R. *et al* 2024 First experimental confirmation of island SOL geometry effects on detachment in Wendelstein 7-X *Nucl. Fusion* submitted
- [34] Feng Y., Beidler C.D., Geiger J., Helander P., Hölbe H., Maassberg H., Turkin Y. and Reiter D. 2016 On the W7-X divertor performance under detached conditions *Nucl. Fusion* **56** 126011
- [35] Schmitz O. *et al* 2020 Stable heat and particle flux detachment with efficient particle exhaust in the island divertor of Wendelstein 7-X *Nucl. Fusion* **61** 016026
- [36] Feng Y. *et al* 2021 Understanding detachment of the W7-X island divertor *Nucl. Fusion* **61** 086012
- [37] Zhang D. *et al* 2021 Plasma radiation behavior approaching high-radiation scenarios in W7-X *Nucl. Fusion* **61** 126002
- [38] Zhang D. *et al* 2021 Bolometer tomography on Wendelstein 7-X for study of radiation asymmetry *Nucl. Fusion* **61** 116043
- [39] Stroth U., Bernert M., Brida D., Cavedon M., Dux R., Huett E., Lunt T., Pan O. and Wischmeier M. (The ASDEX Upgrade Team) 2022 Model for access and stability of the X-point radiator and the threshold for marfes in tokamak plasmas *Nucl. Fusion* **62** 076008
- [40] Lunt T., Bernert M., Brida D., David P., Faitsch M., Pan O., Stieglitz D., Stroth U. and Redl A. 2023 Compact radiative divertor experiments at ASDEX Upgrade and their consequences for a reactor *Phys. Rev. Lett.* **130** 145102
- [41] Pan O., Bernert M., Lunt T., Cavedon M., Kurzan B., Wiesen S., Wischmeier M. and Stroth U. (The ASDEX Upgrade Team) 2022 SOLPS-ITER simulations of an X-point radiator in the ASDEX Upgrade tokamak *Nucl. Fusion* **63** 016001
- [42] Geiger J., Beidler C.D., Feng Y., Maaßberg H., Marushchenko N.B. and Turkin Y. 2014 Physics in the magnetic configuration space of W7-X *Plasma Phys. Control. Fusion* **57** 014004
- [43] Zhang D. *et al* 2019 First observation of a stable highly dissipative divertor plasma regime on the Wendelstein 7-X stellarator *Phys. Rev. Lett.* **123** 025002
- [44] Jakubowski M. *et al* 2021 Overview of the results from divertor experiments with attached and detached plasmas at Wendelstein 7-X and their implications for steady-state operation *Nucl. Fusion* **61** 106003
- [45] Krychowiak M. *et al* 2023 First feedback-controlled divertor detachment in W7-X: experience from TDU operation and prospects for operation with actively cooled divertor *Nucl. Mater. Energy* **34** 101363
- [46] Wesson J. and Campbell D.J. 2011 *Tokamaks* vol 149 (Oxford University Press)
- [47] Feng Y. *et al* 2022 Review of magnetic islands from the divertor perspective and a simplified heat transport model for the island divertor *Plasma Phys. Control. Fusion* **64** 125012
- [48] Hirshman S., van RIJ W.I. and Merkel P. 1986 Three-dimensional free boundary calculations using a spectral Green's function method *Comput. Phys. Commun.* **43** 143
- [49] Feng Y., Sardei F., Grigull P., McCormick K., Kisslinger J. and Reiter D. 2006 Physics of island divertors as highlighted by the example of W7-AS *Nucl. Fusion* **46** 807
- [50] Feng Y. *et al* 2004 3D edge modeling and island divertor physics *Contrib. Plasma Phys.* **44** 57–69
- [51] Reiter D., Baelmans M. and Boerner P. 2005 The EIRENE and B2-EIRENE codes *Fusion Sci. Technol.* **47** 172
- [52] Feng Y., Lunt T., Sardei F. and Zha X. 2013 Implicit coupling of impurity transport at the SOL–core interface *Comput. Phys. Commun.* **184** 1555
- [53] Feng Y. *et al* 2021 First attempt to quantify W7-X island divertor plasma by local experiment-model comparison *Nucl. Fusion* **61** 106018
- [54] Haak V., Bozhenkov S.A., Feng Y., Kharwandikar A., Kremeyer T., Naujoks D., Perseo V., Schlisio G. and Wenzel U. 2023 Overview over the neutral gas pressures in Wendelstein 7-X during divertor operation under boronized wall conditions *Plasma Phys. Control. Fusion* **65** 055024
- [55] Kremeyer T. *et al* 2022 Analysis of hydrogen fueling, recycling and confinement at Wendelstein 7-X via a single-reservoir particle balance *Nucl. Fusion* **62** 036023
- [56] Schlisio G. *et al* 2021 The evolution of the bound particle reservoir in Wendelstein 7-X and its influence on plasma control *Nucl. Fusion* **61** 036031
- [57] Boeyaert D. *et al* 2023 Analysis of the neutral fluxes in the divertor region of Wendelstein 7-X under attached and detached conditions using EMC3-EIRENE *Plasma Phys. Control. Fusion* **66** 015005
- [58] Stroth U., Murakami M., Dory R.A., Yamada H., Okamura S., Sano F. and Obiki T. 1996 Energy confinement scaling from the international stellarator database *Nucl. Fusion* **36** 1063
- [59] Yamada H. *et al* 2005 Characterization of energy confinement in net-current free plasmas using the extended International Stellarator Database *Nucl. Fusion* **45** 1684
- [60] Ringle H., Gasparino U., Kuhner G., Maassberg H., Renner H. and Sardei F. 1990 Confinement studies on the Wendelstein VII-AS stellarator *Plasma Phys. Control. Fusion* **32** 933